frontiers in Materials

ORIGINAL RESEARCH
published: 10 January 2022
doi: 10.3389/fmats.2021.823506

Preparing a Bioactive (Chitosan/Sodium Hyaluronate)/SrHA Coating on Mg–Zn–Ca Alloy for Orthopedic Implant Applications

Yashan Feng[1,2]*, *Lei Chang*[1], *Shijie Zhu*[1], *Yongxin Yang*[1,2], *Baoli Wei*[2], *Meng Lv*[2], *Jun Wang*[1] *and Shaokang Guan*[1]*

[1]School of Materials Science and Engineering, Zhengzhou University, Zhengzhou, China, [2]Biomechanical Engineering Laboratory, Zhengzhou Railway Vocational and Technical College, Zhengzhou, China

The uncontrollable rapid degradation rate of the Mg alloy substrate limited its clinical application, and implant-associated infections have been reported to be the main reason for the secondary surgery of orthopedic implantation. The aim of this study was to produce a multifunctional coating on magnesium-based alloys that have improved corrosion resistance, bioactivity, and antibacterial properties through the preparation of polyelectrolytic multilayers (PEMs) consisting of chitosan (CS) and sodium hyaluronate (HA) on silane-modified strontium-substituted hydroxyapatite (hereafter referred to as Bil (SH + CS)/SrHA). The multifunctional coatings were characterized by scanning electron microscopy (SEM), X-ray diffraction (XRD), Fourier transform infrared spectroscopy (FT-IR), and X-ray photoelectron spectroscopy (XPS). The results showed the polyelectrolyte complex SH/CS layer to be uniformly and tightly attached on to the surface of silane-treated SrHA. At the same time, a potentiodynamic polarization test and hydrogen evolution test showed the Bil (SH + CS)/SrHA coatings to exhibit superior corrosion resistance than bulk Mg-based alloys. The results of the cell–surface interactions revealed Bil (SH + CS)/SrHA coatings to be in favor of cell initial adhesion and more beneficial to the proliferation and growth of cells with the processing of co-culture. In addition, antibacterial tests demonstrated the strong bactericidal effect of Bil (SH + CS)/SrHA coatings against both *Escherichia coli* (*E. coli*) and *Staphylococcus* (*S. aureus*), suggesting that Bil (SH + CS)/SrHA coatings can successfully achieve multifunctionality with enhanced corrosion resistance, biocompatibility, and antibacterial properties.

Keywords: Mg alloys, chitosan, SrHA, bioactive, antibacterial

OPEN ACCESS

Edited by:
Changjiang Pan,
Huaiyin Institute of Technology, China

Reviewed by:
Dan Zou,
Southwest Jiaotong University, China
Xiao Luo,
University of Electronic Science and Technology of China, China
Feng Wu,
Xuzhou University of Technology, China

***Correspondence:**
Yashan Feng
himalaya_2002@163.com
Shaokang Guan
Skguan@zzu.edu.cn

Specialty section:
This article was submitted to Biomaterials, a section of the journal Frontiers in Materials

Received: *27 November 2021*
Accepted: *13 December 2021*
Published: *10 January 2022*

Citation:
Feng Y, Chang L, Zhu S, Yang Y, Wei B, Lv M, Wang J and Guan S (2022) Preparing a Bioactive (Chitosan/Sodium Hyaluronate)/SrHA Coating on Mg–Zn–Ca Alloy for Orthopedic Implant Applications. Front. Mater. 8:823506. doi: 10.3389/fmats.2021.823506

INTRODUCTION

Extensive studies have been conducted on magnesium (Mg)-based alloys in the development of implant materials, especially regarding intravascular stents and bone fixation devices (Yang et al., 2020). More specifically, they possess similar mechanical properties to human bone tissue, in addition to outstanding biodegradable properties (Zheng et al., 2010; Hiromoto et al., 2021; Wang et al., 2021). Mg-based alloys used as an implant material have great potential, but the uncontrollable rapid degradation rate of the substrate remains a significant concern (Hermawan et al., 2010; Song et al., 2018). To enhance the corrosion resistance and bioactivity of Mg alloys, calcium phosphate

(CaP) has been widely studied as the coating ingredient of the Mg alloy substrate (Wang et al., 2010; Gao et al., 2011a; Gao et al., 2011b; Feng et al., 2017). Ionic substitution is an alternative approach for the optimization of the physicochemical properties of CaP coating. Among these substituting ions, Sr^{2+} is an essential micronutrient in bones, and it can lead to an imbalance in bone turnover, which favors formation rather than bone resorption (Ammann et al., 2007; Capuccini et al., 2008) and promotes early angiogenesis (Zhao et al., 2018). Several studies have demonstrated that Sr^{2+}-doped CaP coating exhibits better biocompatibility (Xue et al., 2007), better osteoconductivity (Schrooten et al., 1998; Zarins et al., 2016), and better biological activity (Qiu et al., 2006; Capuccini et al., 2008; Lin et al., 2013). However, it also possesses favorable mechanical properties (Canalis et al., 1996) and a suitable degradation rate (Li et al., 2010). Postoperative infection often results in severe pain and the loss of bone tissue, requiring follow-up treatment. Furthermore, the severe infection can potentially necessitate a second operation (Campoccia et al., 2006). In order to reduce postoperative infection, many studies have attempted to functionalize the antibacterial surface on the Mg alloy substrate (Del Hoyo-Gallego et al., 2016; Geng et al., 2016).

Polyelectrolyte multilayers (PEMs) are considered to be a versatile and convenient membrane synthesis technique for antibacterial surface application (Lichter et al., 2009), which can easily be fabricated using the layer-by-layer (LbL) method. LbL deposition can be achieved by alternating the deposition of oppositely charged polyelectrolytes using electrostatic adsorption. Chitosan (CS) (Feng et al., 2017) and hyaluronate (HA) have gained a great deal of attention in the field of biomedical applications due to the chemical and biological properties they possess. Chitosan is a co-polysaccharide of N-acetyl-D-glucosamine and D-glucosamine, and is known for its biodegradability, bioactivity, and low toxicity. It is a cationic polysaccharide and is positively charged in mildly acidic aqueous, which provides opportunities for the generation of a PEM system. In addition, this positively charged copolysaccharide possesses excellent antibacterial properties by disrupting the negatively charged microbe cell membranes (Savard et al., 2002; Rabea et al., 2003). However, a study has found that the substrate coated with chitosan does not present excellent cytocompatibility *in vitro* fibroblast cultivation (Jou et al., 2007). Sodium hyaluronate is a negatively charged polysaccharide and is the main component of the extracellular matrix. It has been widely investigated for biological application due to its versatile characteristic, such as biocompatibility, biodegradability, non-immunogenicity, and retention properties. CS/HA multilayers have been used as various substrate surface coatings, including titanium (Ti) (Chua et al., 2008), glass (Mulligan et al., 2011), and polypropylene (PP) (Larkin et al., 2010). Recently, Hong et al. prepared SH/CS on the PET artificial ligament, concluding that polysaccharide coating accelerates artificial graft-to-bone healing in the bone tunnel following implantation (Li et al., 2013). Jou et al. attempted to manufacture HA on CS-coated substrate and observed that this composite coating possesses antibacterial activity and also accelerates osteoblast growth.

After considering all the aforementioned factors, this study chose to prepare Bil (SH + CS)/SrHA composite coating on Mg–Zn–Ca substrates. SrHA coating, the inner layer, was designed as a barrier against the rapid corrosion of the substrate during the electrostatic adsorption process, in addition to the implantation period. Bil (SH + CS), the outer layer, was designed to serve as the bioactive surface and provide better corrosion resistance, bioactivity, and antibacterial properties. In order to increase the interfacial adhesion between Bil (SH + CS) and SrHA, silane (KH792) was covalently immobilized on to SrHA. The amino of functionalized SrHA easily combined with H^+ in the solution and generated NH_3^+, carrying a positive charge and was beneficial for the electrostatic absorption. An evaluation of the physiochemical properties of Bil (SH + CS)/SrHA coatings, including microstructure, elemental composition, corrosion resistance, *in vitro* cytocompatibility, and antibacterial activity, was then conducted.

EXPERIMENTAL AND METHOD

Preparation of SrHA Coating

Mg–Zn–Ca alloys that were developed in our lab (Henan Provincial Key Laboratory of Advanced Magnesium Alloy) were chosen as substrate coating. The as-cast ingots were cut into rectangular plates measuring 25 mm × 10 mm × 4 mm. All samples were then grounded and polished with silicon carbide papers of 200 to 1,000 grids, followed by ultrasonic cleaning in acetone–ethanol solution for 10 min. Samples were then rinsed in deionized water and air-dried. SrHA coatings were directly synthesized on the surface of Mg–Zn–Ca substrates using the electrodeposition technique provided by the electrochemical workstation (RST5200, KeRui Instruments, China). Samples, platinum plate, and saturated calomel electrode were used as the working, counter, and reference electrodes, respectively. The electrolyte was prepared by dissolving 0.021 mol/L $Ca(NO_3)_2{\cdot}4H_2O$, 0.025 mol/L $NH_4H_2PO_4$, 0.021 mol/L $Sr(NO_3)_2$, and 0.1 mol/L $NaNO_3$ into deionized water at room temperature. The pH value of the electrolyte was adjusted to 5.0 using diluted $(CH_2OH)_3CNH_2$ and HNO_3. All reagents were of analytical grade. The detailed electrical parameters were optimized and published in our previous study (Wang et al., 2010). Following the deposition, samples were rinsed in deionized water and then air-dried.

Silane Treatment

KH792 was used as a silane-coupling agent as a means of increasing the interfacial adhesion between Bil (SH + CS) and SrHA layers. Deionized water was added to ethanol with a volumetric ratio of 15:85, and the mixed solution was adjusted to pH = 5.0 using glacial acid to catalyze the hydrolysis. 0.5 g KH792 was then dripped into the aqueous ethanol solution (100 ml), which was then stirred at 25°C for 1 h. SrHA-coated samples were then immersed into the KH792 solution at 65°C in a magnetic stirrer for 12 h. Following the reaction, the samples were rinsed in ethanol and deionized water before being cured for 12 h at 80°C in an oven.

Preparation of Bil (SH + CS) Coating

Chitosan powder (CS, Aladdin, China, 179.17) was dissolved in aqueous acetic acid solution (pH 5.6, Aladdin, China) to produce CS stock solution (1 mg/ ml). Sodium hyaluronate (HA, Aladdin, China, 403.3) was dissolved in deionized water to produce HA stock solution (1 mg/ ml). Both solutions were then stored in a fridge overnight after preparation. Silane-treated SrHA samples were first dipped into the HA solution and then chitosan solution for 10 min each, before being rinsed with acetic buffer solution and air-dried. The alternating polyelectrolyte deposition cycle was continued for five bilayers.

Coating Characterization

Structural and compositional measurements of the SrHA and silane-treated SrHA were taken using X-ray diffraction (XRD, Philips 1700X, Netherlands), Fourier transform infrared spectroscopy (FTIR, SPM-9500 J3, Japan), and X-ray photoelectron spectroscopy (XPS, PHI Quantera SXM, Japan). An XRD analysis was performed using Cu Kα1 radiation at a scan rate of 4°/minute. The FTIR spectrum of the coatings was recorded in a range of 4,000–500 cm^{-1}. Regarding the operating details of XPS, an Al Kα radiation source was employed with scanning energy of 1 and 0.1 eV for the survey and a high-resolution scan, respectively. XPS binding energy (BE) values were charge-corrected after setting the C 1s hydrocarbon component to 284.8 eV. Coating morphology was examined by a scanning electron microscope (SEM, Quanta-200, Netherlands) that was equipped with EDS.

Zeta Potential Measurement

The zeta-potential was examined by a solid potentiometer (SurPASS 3, Anton Paar, Austria) at room temperature. The zeta potential of each sample was measured three times, and the average values were reported.

Corrosion Test

Corrosion resistance of the samples was evaluated using potentiodynamic polarization and electrochemical impedance spectroscopy (EIS). They were conducted at 36.5 ± 0.5°C in simulated body fluid (Kokubo and Takadama, 2006). Each sample was sealed using two-component epoxy with an exposure area of 1.0 cm^2 (1.0 cm × 1.0 cm). Potentiodynamic polarization tests were conducted in a three-electrode cell. A platinum plate was used as the counter-electrode, and a saturated calomel electrode was used as the reference electrode. All measured potential values were related to the SCE.

Cell Adhesion and Morphology

Mesenchymal stem cells (MSCs) were isolated from Sprague–Dawley male rats and cultured in Dulbecco's modified Eagle's medium (DMEM, Sigma, United States) that was supplemented with 10% fetal bovine serum (PBS, Sigma, United States) and 1% penicillin–streptomycin (P/S, Sigma, United States) at 37°C in a humidified atmosphere that contained 5% CO_2 and 95% air. All samples used during the cell adhesion experiments were initially disinfected by ultraviolet radiation. When MSCs covered approximately 80% of the bottom area of the culture dish, cells were seeded to the coating surfaces (SrHA and Bil (SH + CS)/SrHA) and a blank plate (control group) with a seeding density of 1 × 10^4 cells/ml. Medium changes were conducted every 2 days, and the culture period was set as 4 h, 1 day, and 5 days. At each of these time points, the coated samples were removed from the culture medium and fixed by adding 2.5% glutaraldehyde (Aladdin, China) for 2 h at room temperature before being dehydrated in ethanol series (50, 70, 90, and 100%) at 10 min per grade, and eventually being substituted with hexamethyldisilazane (HMDS, Sigma, United States) before being air-dried. All the samples were then sputter-coated with gold prior to SEM observation.

Immunocytochemistry

Cell cytoskeleton was observed using the FITC-labeled phalloidin (40735ES75, Yesen, China). At 4 h and 1 day, the medium was removed by aspiration, and cells on the coatings were fixed with 4% paraformaldehyde in 1 × PBS for 20 min at room temperature before being washed twice with 1 × PBS. Cells were then permeabilized with 0.5% Triton 1 × PBS for 5 min, and then blocked with 1% (w/v) solution of bovine serum albumin (BSA, Sigma-Aldrich) in 1 × PBS for 1 h at room temperature. Actin filaments were then labeled by FITC-labeled phalloidin for 30 min at room temperature. Samples were then washed twice (5 min each time) with 1 × PBS. Visualization was then conducted using a Nikon microscope (Ti-E, Nikon, Japan). FITC-labeled phalloidin was excited at 488 nm.

Antibacterial Activity

Escherichia coli (*E. coli*) and *Staphylococcus aureus* (*S. aureus*) were used for evaluating the antibacterial efficacy of samples using the plate-counting method. All samples were initially sterilized using ultraviolet radiation, and then 5 ml agar culture medium was spread across the surface of each sample. Following agar solidification, 1 ml of each bacterium solution (1 × 10^6 CFU cm^{-1}) was inoculated on the agar plate before the polyethylene film was placed onto the seeded agar plate and incubated at 37°C for 24 h. At the end of the time point, samples were washed repeatedly to facilitate eluent collection, and the number of bacteria colonies was counted.

Statistical Analysis

One-way ANOVA with Tukey's *post hoc* test was used for determining any significant differences that existed between the mean values of the experimental groups using Prism® version 5 (GraphPad, California). Difference between groups was considered significant at the 95% confidence interval. Three replicates were measured, and mean values were then calculated.

RESULTS

Composition Investigation of Silane-Treated SrHA

The typical XRD patterns of samples that were coated with SrHA and silane-treated SrHA can be seen in **Figure 1A**. It is apparent that the diffraction peak corresponding to the (002) crystal plane

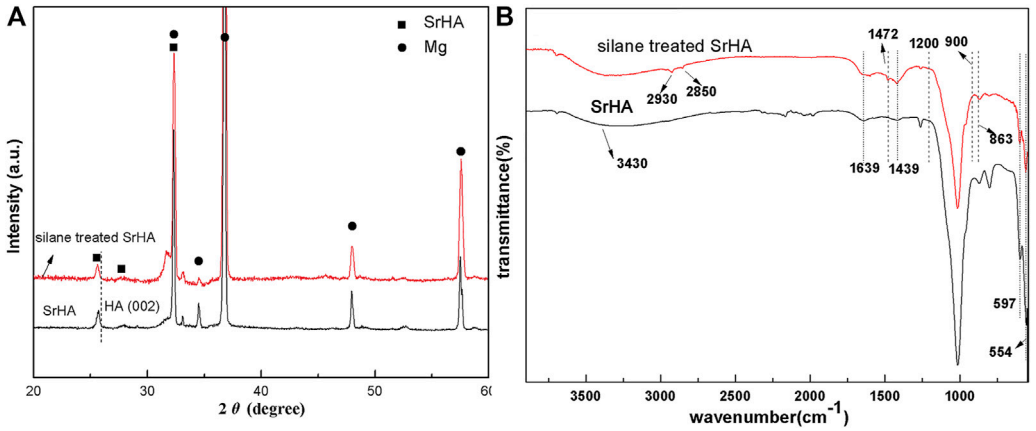

FIGURE 1 | XRD pattern **(A)** and FTIR spectra **(B)** of the as-synthesized samples coated with SrHA and silane-treated SrHA.

(characteristic peak of SrHA prepared by electrodeposition) significantly shifts to a smaller angle compared to that of pure HA. This can be attributed to the higher ionic radius of Sr compared to Ca. The X-ray diffraction analysis of the KH792-treated SrHA exhibited identical peaks to those of SrHA, thereby confirming that KH792 treatment does not affect the SrHA crystal structure. In addition, functionalized SrHA is only distributed in the outermost layers of SrHA, and the amount is far too little to display any prominent peak to confirm functionalization.

The FTIR spectra of SrHA and silane-treated SrHA can be seen in **Figure 1B**. In the SrHA spectrum, the bands of 900–1,200 cm^{-1}, 554 cm^{-1}, and 597 cm^{-1} can be attributed to the phosphate bond (Sun et al., 2015). The bands associated with the stretching modes of CO_3^{2-} can be observed at 1,439 cm^{-1} and 863 cm^{-1} (Zhang et al., 2014). The bands of 3,430 cm^{-1} and 1,639 cm^{-1} arise from OH^- and HPO_4^{3-}, respectively. In the FTIR spectra of silane-treated SrHA, in addition to the presence of characteristic peaks of SrHA, the spectrum exhibits new peaks at 2,930 cm^{-1} and 2,850 cm^{-1} (C-H stretching) and 1,472 cm^{-1} (hydrogen-bonded NH_2 deformation) (Rehman et al., 2016), strongly confirming the functionalized SrHA. In this study, N-(β-aminoethyl)-γ-aminopropyltrimethxy silane (KH792) was used as the silane-coupling agent. During treatment, the -Si(OH)$_3$ group, the hydrolysis product of KH792, chemically reacted with PO_4^{3-} or OH^- ions of SrHA and formed -Si–O- and Si–O–P chemical bonds, respectively. In the spectrum of silane-treated SrHA coatings, no obvious stretching peak associated to the band of Si–O–P at 998 cm^{-1} can be observed, potentially as a result of overlapping with the band of PO_4^{3-}.

For more accurately determining the chemical composition of the KH792 functionalized SrHA, XPS measurement was conducted, the results of which can be seen in **Figure 2**. According to the survey spectra, the surface of silane-treated SrHA coatings contains Si, N, O, Mg, Ca, Sr, P, and C, further verifying the chemical reaction between KH792 and SrHA. In the silane treatment process, Mg–Zn–Ca substrates were corroded slightly and Mg was still detectable in the survey scan of the coating. As is shown in **Figure 2B**, the Si2p spectra are separated into four peaks. The first peak is located at 102.49 eV and is attributed to Si-OH (Ramezanzadeh et al., 2016). The second peak, which is at 101.95 eV, corresponds to the Si–O–Si bonding of KH792-treated SrHA (Lee et al., 2015). The third peak at 100.20 eV is assigned to Si–C bonding. The presence of Si–O–P at 530.6 eV confirms the successful functionalization of SrHA. The spectrum of O 1s can be deconvoluted into five peaks. Those corresponding to Si–O (532.8 eV) and C–O (532.2 eV) are assigned to O 1s in functioned SrHA (Lee et al., 2015; Ramezanzadeh et al., 2016; Zhu et al., 2016), and the peaks that are found at 531.3 eV and 532.8 can be attributed to the PO_4^{3-} group and the OH^- group in SrHA (Wang et al., 2010). The C 1s (**Figure 2D**) spectra were fitted to four peaks at 286.1, 285.6, 283.8, and 284.7 eV, which are associated with the bonding of C–N, C–O, C–Si, and C–C.

FTIR Analysis of Bil (SH + CS)/SrHA Coating

Figure 3 displays the representative spectra of Bil (SH + CS)/SrHA, in addition to pure CS and HA on SrHA. In the Bil (SH + CS)/SrHA spectrum, the phosphate bond at 900–1,200 cm^{-1}, 554 cm^{-1}, and 597 cm^{-1}, and O–H located at 3,000–3,700 cm^{-1} were observed. However, the peaks corresponding to HPO_4^{2-} and CO_3^{2-} were not detected, potentially as a result of detection limits. The spectrum of sodium hyaluronate exhibited several bands at 2,580–2,940 cm^{-1} and 3,100–3,600 cm^{-1}, and they are associated with the bond of–CH_2– and the overlap of–OH and N–H (Umerska et al., 2012). The highly overlapping bands in the region of 1800–1,500 cm^{-1} come from the acetamide and carboxylate group (Servaty et al., 2001). The highest peak at 1,609 cm^{-1} is attributed to the asymmetrical stretching vibration of the carboxylate (COO^-) (Servaty et al., 2001; Dřímalová et al., 2005). Overlapped with this peak was the amide I and amide II bonds of the acetamide group, corresponding to 1,648 cm^{-1} and 1,556 cm^{-1}, respectively (Servaty et al., 2001). As can be seen in the chitosan spectrum, the band at 1,656 cm^{-1} is attributed to the C=O of the amide group in acetylated chitosan units. The band at 1,586 cm^{-1} is assigned to the amide group and N–H bending vibration of the amine group in deacetylated units. From

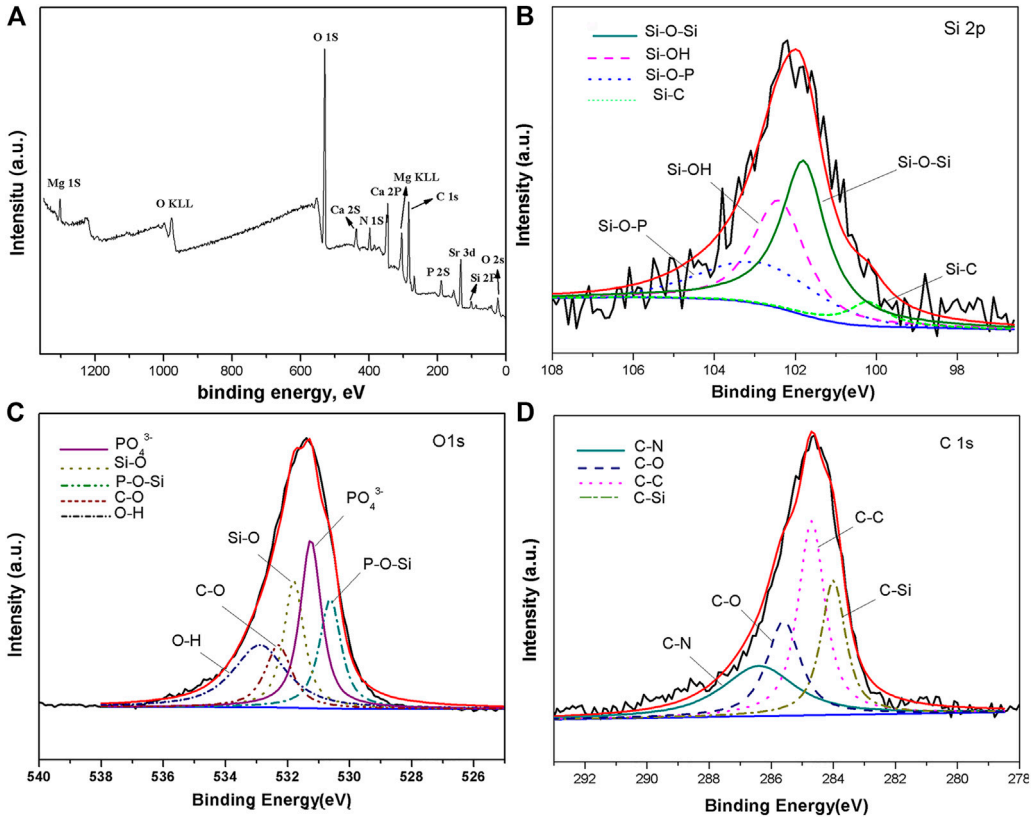

FIGURE 2 | XPS survey spectrum **(A)** and high-resolution spectra of **(B)** Si 2p, **(C)** O 1s, **(D)** and C 1s of silane-treated SrHA coating.

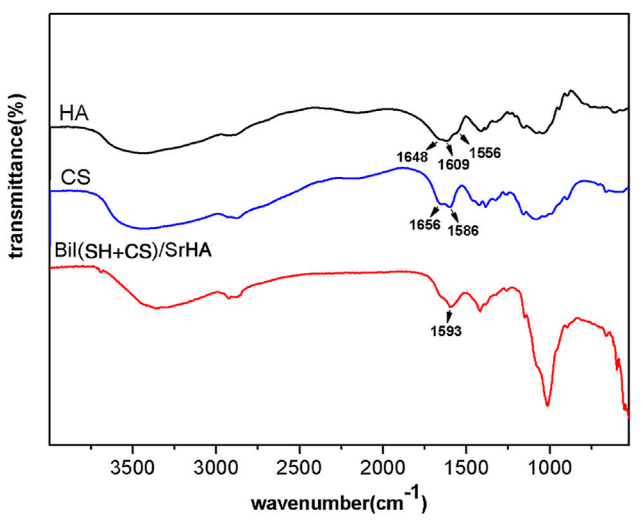

FIGURE 3 | FTIR spectra of the CS, HA, and Bil (SH + CS) on silane-treated SrHA.

Figure 3, it can be seen that the peaks in the region of 1700 cm^{-1} to 1,500 cm^{-1} of Bil (SH + CS)/SrHA spectrum were relatively changed from the CS and HA spectrum, which presents an overlapped peak of the carbonyl and amide vibrations of both polysaccharides at 1,593 cm^{-1}.

Corrosion Properties

Representative potentiodynamic polarization curves of the specimens can be seen in **Figure 4A**. The E_{corr} of SrHA-coated samples is approximately −1.62 V and that of Bil (SH + CS)/SrHA-coated Mg alloy exhibits the positive shift to −1.54 V, which indicates an enhancement of the corrosion resistance. At the same time, the I_{corr} of Bil (SH + CS) coating is an order of magnitude lower than the SrHA-coated sample, demonstrating a decline from $\times 1.3610^{-5}$A/ cm^2 to 2.65 × 10^{-6} A/ cm^2. The hydrogen evolution curves of the samples in SBF solution are shown in **Figure 4B**. As the figure shows, a small amount of H_2 was generated from the coated samples, and Bil (SH + CS)/SrHA coatings presented the lowest hydrogen evolution amount, indicating that the Bil (SH + CS)/SrHA coating highly improved corrosion resistance of the Mg alloy substrate.

Cell Adhesion and Cytoskeletal F-Actin Development

The initial adhesion morphology of MSCs cultured on SrHA coatings and Bil (SH + CS)/SrHA coatings for 4 and 24 h were observed by SEM, and the typical images can be seen in **Figure 5**. As **Figures 5A,C** show, MSCs were attached and spread well on

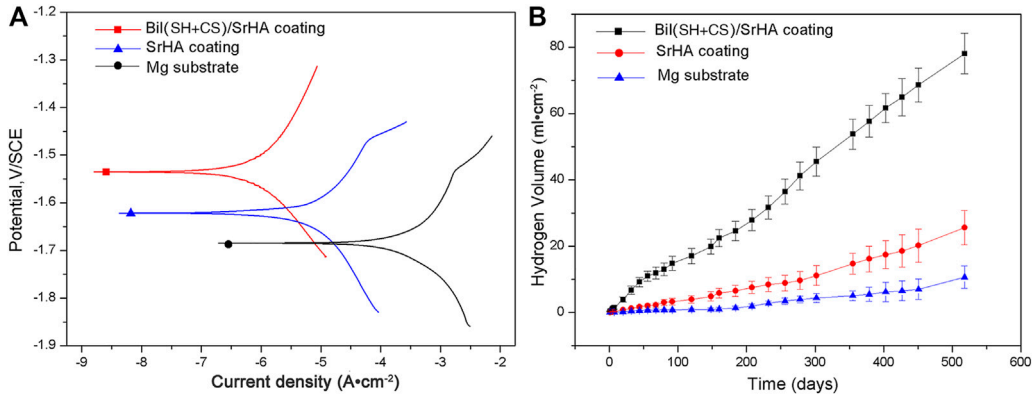

FIGURE 4 | Polarization curves **(A)** and hydrogen evolution volume **(B)** of Mg substrate, SrHA coating, and Bil (SH + CS)/SrHA coating.

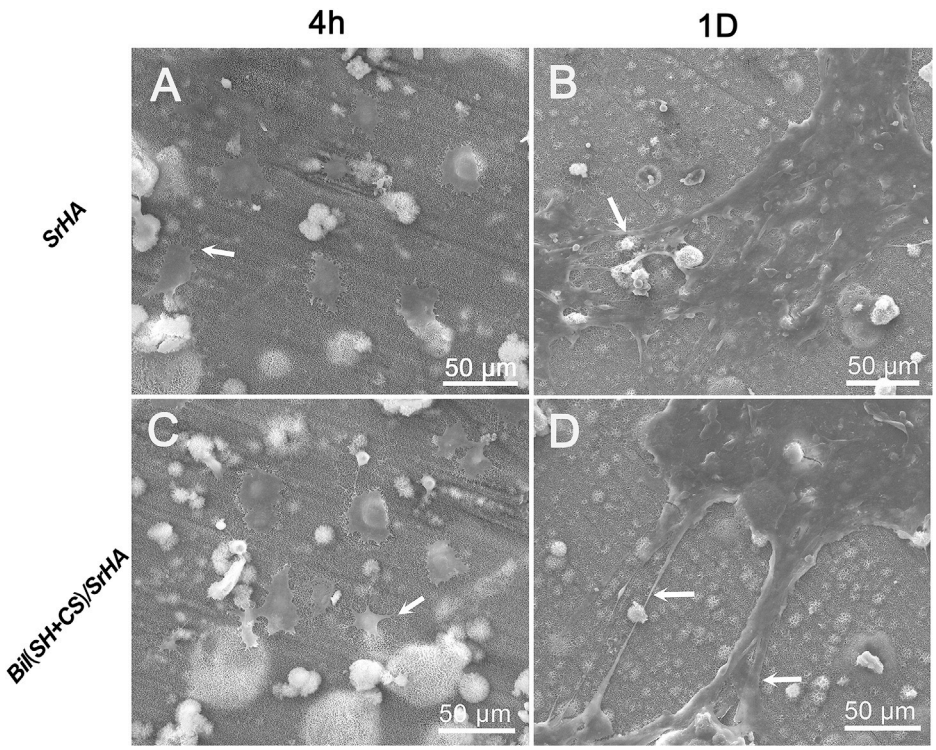

FIGURE 5 | Cell attachment and adhesion on different samples at various times: Cells cultured on SrHA-coated sample for 4 h **(A)** 24 h **(B)**; Cells cultured on Bil (SH+CS)/SrHA-coated sample for 4 h **(C)** 24 h **(D)**.

two coating types, with tiny filopodia extended from the cell edges. After being cultured for 24 h, there was more pronounced cell spreading on coatings and flattened patterns covered the coating surface (**Figures 5B,D**). **Figure 6** displays the fluorescent microscopy images of cytoskeletal organization of MSCs on coatings during the initial 24 h. **Figure 6A** shows that the cell cytoskeleton on the culture dish (control group) presented the polygon structure, and this increased as incubation time was extended (**Figure 6D**). Compared to the control group, the cytoskeletal on coated samples presented a snow-like structure (**Figures 6B,C**), which indicates that a large number of prominent filopodia anchored the cell body on the coatings. After being cultured for 24 h, the MSCs on the coated samples grew, proliferated, and overlapped with each other (**Figures 6E,F**). It is noticeable that cellular filopodia are extending, which indicates cell growth and migration on the coating surface.

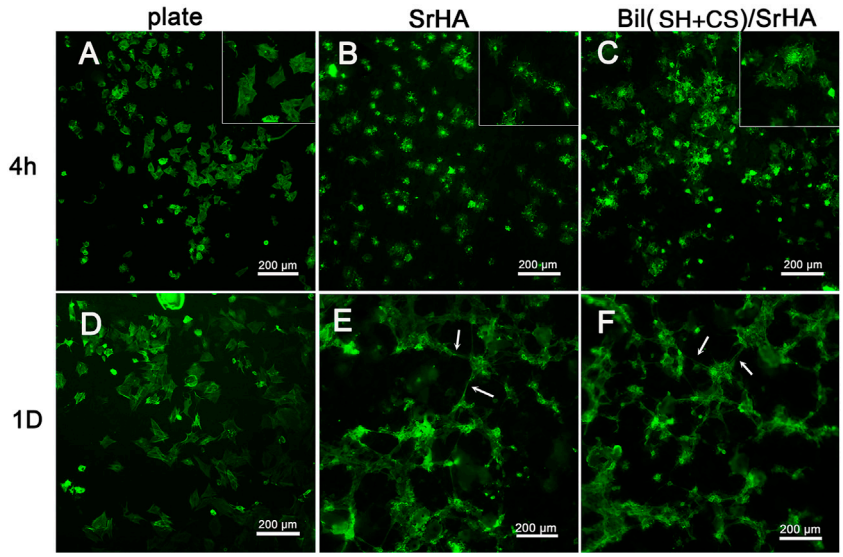

FIGURE 6 | Morphology of MSCs revealed by immunofluorescence staining of cytoskeletal F-actin: Cells cultured on plate for 4h **(A)**, 1D **(D)**; Cells cultured on SrHA-coated sample for 4h **(B)**, 1D **(E)**; Cells cultured on Bil(SH+CS)/SrHA-coated sample for 4h **(C)**, 1D **(F)**.

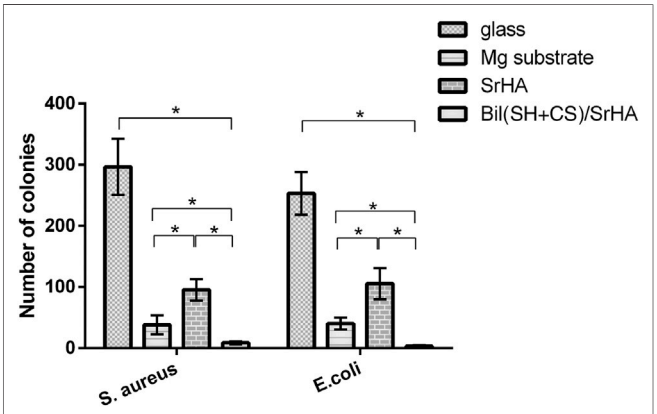

FIGURE 7 | Antibacterial properties and biocompatibility of Mg substrate, SrHA, and Bil (SH + CS)/SrHA, *represents $p < 0.05$.

In Vitro Antibacterial Properties

The antibacterial effects of the coated samples against *S. aureus* and *E. coli* were evaluated using the spread plate count method. **Figure 7** shows the number of adherent colonies on the sample surface following 24 h of incubation. Significant differences in the colony number of attached bacteria were observed between the control group (glass) and Bil (SH + CS)/SrHA coatings, showing a reduction of 300 times and 260 times in *S. aureus* and *E. coli* on Bil (SH + CS)/SrHA coatings. Regarding the Mg–Zn–Ca substrates, the inhibiting effect was also observed, but there was weaker efficacy than that of Bil (SH + CS)/SrHA coatings. Bacteria growth was partially inhibited on SrHA coatings, and more than 10^2 colonies were still adhered to the surface.

However, Bil (SH + CS)/SrHA coatings have clearly demonstrated antibacterial properties over the other groups (Mg–Zn–Ca substrates and SrHA coatings) in the prevention of initial bacterial adhesion, resulting in biofilm minimization.

DISCUSSION

One of the most common reasons for orthopedic implant failure is implant-associated bacterial infection, and this can lead to antibiotic inefficacy and the eventual removal of an implant. Mg-based alloys have been reported to display excellent antibacterial activity and are regarded as being a potential biodegradable material for orthopedic application. However, the rapid degradation rate and consequent metallic ion release from alloying elements significantly affect durability and cytotoxicity, meaning there is also impedance to clinical practice. Surface modification is the most effective approach for simultaneously improving corrosion resistance and bioactivity of Mg-based alloys.

The aim of this study was controlling the rapid degradation of Mg-based alloys through the construction of a dense multilayer coating structure, utilizing the electrodeposition technique for producing the barrier layer with sufficient bonding strength to the substrate, and sealing the exposed micro-surface of the substrate using the layer-by-layer technique as a means of further enhancing corrosion resistance. The composition of this coating was created using SrHA, chitosan, and sodium hyaluronate, ensuring intensive bioactivity and antibacterial efficacy. Sr-containing coatings have been reported to activate osteoblast cell replication, inhibit bone resorption, and improve

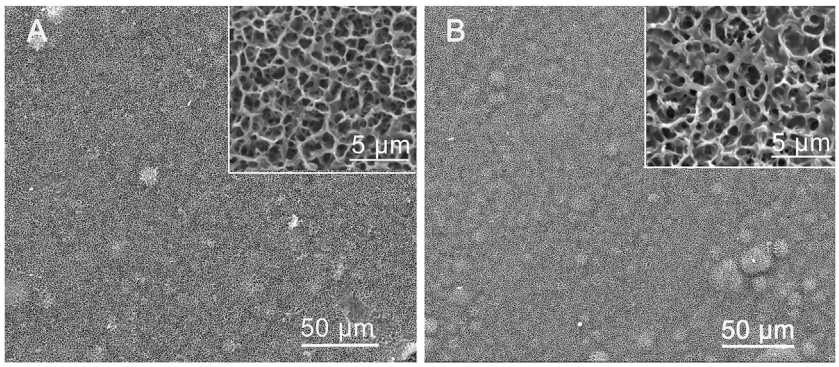

FIGURE 8 | SEM images of the surface of SrHA coating **(A)** and Bil (SH + CS)/SrHA coating **(B)**.

bone–implant integration (Li et al., 2010; Chen et al., 2014; Lin et al., 2014; Singh et al., 2014), and Sr-containing coatings have been reported to form on magnesium alloys through either electrodeposition or micro-arc oxidation techniques (Lin et al., 2014). However, the key issue with the multilayer coating structure is the integrity between SrHA and PEMs (self-assembled chitosan and sodium hyaluronate). In order to solve this issue, silane treatment was applied on the top of the SrHA layer, making it possible to provide electric charge to the coating surface and strengthening the interfacial adhesion between SrHA and PEMs. Therefore, the influence of silane treatment on Bil (SH + CS)/SrHA coatings was discussed, the coating formation mechanism was proposed, and an exploration of the effect of Bil (SH + CS)/SrHA coatings on antibacterial property and bioactivity was conducted.

Generally, SrHA crystal structure stability was retained following silane treatment, and no additional diffraction peak can be observed in **Figure 1A**. The presence of C–H stretching peaks (at 2,930 cm^{-1} and 2,850 cm^{-1}), in addition to the hydrogen-bonded NH_2 deformation peak (at 1,472 cm^{-1}), in the spectrum of silane-treated SrHA demonstrated the functionalization of SrHA. As a means of further proving the chemical reaction between the silane agent (KH792) and the SrHA layer, the XPS survey was conducted, and the presence of the Si–O–P bond at 530.6 eV (as can be seen in **Figure 2**) supported the bonding mechanism between the silane agent and the SrHA layer. The role of silane treatment is the initialization of the follow-up reaction with HA and strengthening of the bonding between SrHA and PEMs without producing any adverse effects. Regarding the PEMs, an overlapped peak belonging to the carbonyl and amide vibrations of both polysaccharides (at 1,593 cm^{-1} in **Figure 3**) was observed in the Bil (SH + CS)/SrHA spectrum rather than the typical peaks of HA and CS ranging from 1700 cm^{-1} to 1500 cm^{-1}. This phenomenon is attributed to the shift of the asymmetrical stretching vibration of the carbonyl group from sodium hyaluronate or the N–H bending vibration of the amine group of chitosan and can be interpreted as being a sign of electrostatic interaction of the carboxylate group and the NH^{3+} group in both polysaccharides. **Figure 8** illustrates the morphologies of SrHA and the Bil (SH + CS)/SrHA coatings. This shows that SrHA coatings (**Figure 8A**) present a network structure, which is beneficial for cell adhesion. From **Figure 8B**, it can be seen that the low magnification image of Bil (SH + CS)/SrHA displays no significant difference with pure SrHA coating, and the surface is dense and uniform, exhibiting no cracks. At the same time, the SrHA network structure appears to be wrapped with the polymer shells at higher magnification. From the evaluation of corrosion resistance, it can be seen that Bil (SH + CS)/SrHA coatings greatly improved the corrosion resistance compared to Mg–Zn–Ca alloys and the SrHA layer. In addition, the protective efficacy of Bil (SH + CS)/SrHA coatings is validated for a longer duration (as can be seen in **Figure 4**). The reason for this could be the sealing effect of PEMs to the SrHA layer. In the electrodeposition process, SrHA particles were precipitated and then stacked on the substrate surface, and the microstructure possibly hindered corrosion resistance. HA/CS was then bonded to the silane-treated SrHA particles, and the PEM structure was ultimately formed, similar to a polymer shell (SH + CS). The polymer shell (SH + CS) could contribute to the sealing effect of the exposed micro-surface, thereby protecting the substrate coated

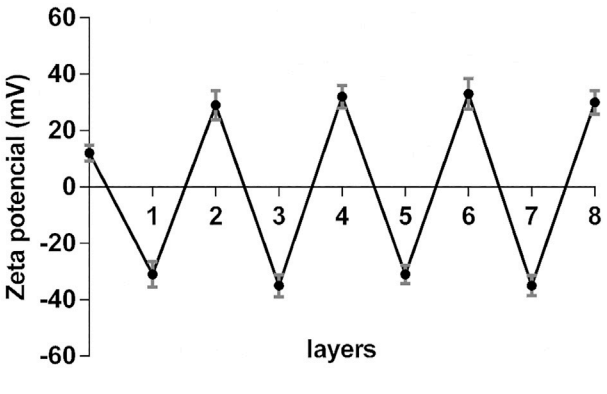

FIGURE 9 | Zeta-potential surface charge alternation with the deposition of each polyelectrolyte layer. 0 layers corresponded with the SrHA layer following silane treatment.

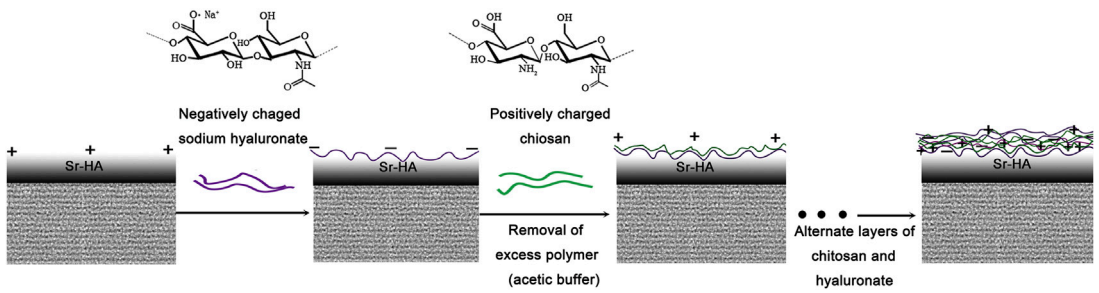

FIGURE 10 | Schematic illustration of the formation process of the deposition of chitosan and sodium hyaluronate on KH792-treated SrHA.

with SrHA from SBF corrosion. This hypothesis could be supported by the morphology evolution that is shown in **Figure 8**.

In order to further understand the reaction between silane-treated SrHA and PEMs, the coating formation mechanism was discussed. **Figure 9** shows the surface zeta potential of each polyelectrolyte layer of Bil (SH + CS)/SrHA. The ζ-potential of SrHA following silane treatment (0 layers) increased to 16 mV, contributing to the effective attachment of the $-NH_2$ group to the surface. The general trend is that odd layers have a negative charge, whereas the even layers have a positive charge. Following discussion, the formation mechanism of Bil (SH + CS)/SrHA coating was proposed (**Figure 10**). The positively charged SrHA surface following silane treatment reacted with HA, and the residual carboxylic acid groups in HA caused a decrease in zeta-potential, as shown in **Figure 9**. After being immersed in CS solution, the cationic nature of CS molecules caused a sharp increase in zeta potential, and the alternative interaction between positive and negative charges on the surface ultimately formed the Bil (SH + CS)/SrHA coating. In addition, the excess gel of the HA and CS was rinsed using an acetic buffer. As the multilayered (SH + CS) coatings involved organic monolayer assembly by polyelectrolytes and van der Waals interaction, the polyelectrolyte complex layer was tightly attached to the charged SrHA. This can be anticipated to be more stable than the conventional dip coating process. It has been demonstrated that the Bil (SH + CS) coating uniformly wraps on the silane-treated SrHA, effectively delaying the corrosion of the samples that are coated with SrHA (as can be seen in **Figure 4**).

Orthopedic application coatings must be bioactive and antibacterial, effectively inhibiting infection and simultaneously improving bone growth at the bone–implant interface, which can achieve a faster bone healing process (Chang et al., 2013; Lim et al., 2014; Lim et al., 2015). This coupling effect is essential, and Bil (SH + CS)/SrHA coating was designed to provide such a unique function. Relatively few studies have been conducted on the antimicrobial properties of the Mg–Zn–Ca alloy substrate. However, as shown in **Figure 7**, the Mg alloy substrate exhibits potent activities against Gram-positive and Gram-negative bacteria. During the process of the spread-plate method experiment, as the agar was poured into the substrate surface, the pH of the agar increased due to the abundance of OH^- that was produced by Mg corrosion. Therefore, the pH of the agar environment is unsuitable for the bacterial infection. Regarding the SrHA-coated samples, SrHA has not been proven to be antibacterial, as previous studies have demonstrated (Geng et al., 2016; Huang et al., 2016). In addition, SrHA enhanced Mg alloy substrate corrosion resistance to a certain degree, which could decrease the influence of the pH to the bacterial infection. Regarding Bil (SH + CS)/SrHA coatings, it is widely known that chitosan is an excellent antibacterial material. Chitosan can enter microbial cells through the cell membrane, combining with

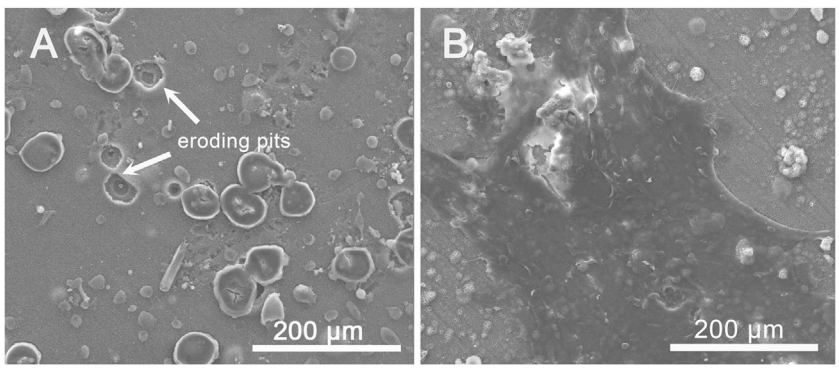

FIGURE 11 | SEM images of cell morphology on day 5 of co-culture with **(A)** SrHA and **(B)** Bil (SH + CS)/SrHA.

negatively charged substances (mostly proteins and nucleic acids) in the cells, thereby affecting their normal physiological functions (including DNA replication and protein synthesis), which results in microbial death. Furthermore, the interaction that occurs between the positive charge of chitosan and the negative charge on the surface of the microbial cell membrane changes the permeability of the microbial cell membrane, which contributes to microbial cell death. Results demonstrated that Bil (SH + CS)/SrHA coatings exhibited a good inhibition effect toward both *S. aureus* and *E. coli* during the incubation period.

In order to demonstrate the bioactivity of Bil (SH + CS)/SrHA coatings, MSCs were cultured directly on the coating surface *in vitro*. **Figure 5** proves that both the SrHA coatings and Bil (SH + CS)/SrHA coatings are favorable for the initial adhesion, proliferation, and spreading of MSCs, and no obvious difference was exhibited. Preliminary studies have shown that the surface properties of the coating, including surface topography, surface chemistry, surface wettability, and surface energy would significantly influence cell–material interactions. In addition, extensive *in vitro* studies have proven that the adhesion, morphology, and mineralization of osteoblasts are sensitive to nano-scale features (Hovgaard et al., 2008; Olivares-Navarrete et al., 2008). The cell patterns of SrHA and Bil (SH + CS)/SrHA following 5 days of culturing can be seen in **Figure 11**. MSCs grew and spread across the entire surface of Bil (SH + CS)/SrHA coatings, whereas cells on SrHA coatings shrunk, which indicates that the cells grew poorly and may have completely stopped dividing. In addition, many eroding pits were observed on the SrHA coating. As cell cultivation proceeded, SrHA-coated samples corroded intensively, which led to an increase in the pH value, potentially hindering cell growth and proliferation.

In this study, the surface chemistry and surface charge of Bil (SH + CS)/SrHA coating changed compared to that of SrHA coating, but the surface morphology remained similar due to the thinness of polyelectrolyte multilayer coating (**Figure 8**). **Figure 5** displays no obvious difference in terms of cell adhesion and distribution, so the adhesion and cytoskeletal development of MSCs on samples may be determined primarily by surface topography during the initial stage. This phenomenon is consistent with the findings of previous reports (Ding et al., 2015). Although SrHA coatings are favorable for the initial adhesion of MSCs, relatively poor corrosion resistance hindered the growth of MSCs during the long culturing period. Therefore, the composite Bil (SH + CS)/SrHA coatings are more suitable for cell adhesion and proliferation due to their improved corrosion resistance.

CONCLUSION

This study focused on the preparation and preliminary study of a bioactive and antibacterial composite coating (Bil (SH + CS)/SrHA) on Mg–Zn–Ca alloys. As evidenced by XRD and FTIR analyses, amino groups were successfully covalent bonded to the SrHA coating surface. SH/CS was built up on silane-modified SrHA coating based on the layer-by-layer assembly and was confirmed by observing zeta-potential. According to electrochemical studies and the hydrogen evolution experiment, Bil (SH + CS)/SrHA exhibited better corrosion resistance than SrHA, which presents one order of magnitude decrease in I_{corr}. The cell adhesion tests revealed Bil (SH + CS)/SrHA coatings to be more beneficial for the proliferation and growth of cells, due to the better corrosion resistance. In the antibacterial test, the Bil (SH + CS)/SrHA exhibited significant antibacterial efficacy, particularly in comparison to SrHA. Therefore, Mg–Zn–Ca substrates coated with Bil (SH + CS)/SrHA exhibited excellent biocompatibility and superior antibacterial abilities, making them more effective for biomedical applications.

DATA AVAILABILITY STATEMENT

The raw data supporting the conclusions of this article will be made available by the authors, without undue reservation.

AUTHOR CONTRIBUTIONS

YF and SG undertook the design, guidance, and modification of this project and manuscript. YF completed the implementation of the project and writing of the manuscript, and other authors completed the collection and collation of data.

FUNDING

This work was supported by the National Natural Science Foundation of China (U1804251), Key Research and Development Program of China (2018YFC1106703), Key Research and Development Special Project of Henan Provincial Science and Technology (No. 202202310088), National Youth Fund (No.51601169), and Major Science research Project of high Education of Henan Province (22B430033).

REFERENCES

Ammann, P., Badoud, I., Barraud, S., Dayer, R., and Rizzoli, R. (2007). Strontium Ranelate Treatment Improves Trabecular and Cortical Intrinsic Bone Tissue Quality, a Determinant of Bone Strength. *J. Bone Miner Res.* 22, 1419–1425. doi:10.1359/jbmr.070607

Campoccia, D., Montanaro, L., and Arciola, C. R. (2006). The Significance of Infection Related to Orthopedic Devices and Issues of Antibiotic Resistance. *Biomaterials* 27, 2331–2339. doi:10.1016/j.biomaterials.2005.11.044

Canalis, E., Hott, M., Deloffre, P., Tsouderos, Y., and Marie, P. J. (1996). The Divalent Strontium Salt S12911 Enhances Bone Cell Replication and Bone Formation *In Vitro*. *Bone* 18, 517–523. doi:10.1016/8756-3282(96)00080-4

Capuccini, C., Torricelli, P., Sima, F., Boanini, E., Ristoscu, C., Bracci, B., et al. (2008). Strontium-substituted Hydroxyapatite Coatings Synthesized by Pulsed-Laser Deposition: *In Vitro* Osteoblast and Osteoclast Response. *Acta Biomater.* 4, 1885–1893. doi:10.1016/j.actbio.2008.05.005

Chang, L., Sun, J., Fuh, J. Y. H., and Thian, E. S. (2013). Deposition and Characterization of a Dual-Layer Silicon- and Silver-Containing Hydroxyapatite Coating via a Drop-On-Demand Technique. *RSC Adv.* 3, 11162–11168. doi:10.1039/c3ra23251d

Chen, X. B., Nisbet, D. R., Li, R. W., Smith, P. N., Abbott, T. B., Easton, M. A., et al. (2014). Controlling Initial Biodegradation of Magnesium by a Biocompatible Strontium Phosphate Conversion Coating. *Acta Biomater.* 10, 1463–1474. doi:10.1016/j.actbio.2013.11.016

Chua, P.-H., Neoh, K.-G., Kang, E.-T., and Wang, W. (2008). Surface Functionalization of Titanium with Hyaluronic Acid/chitosan Polyelectrolyte Multilayers and RGD for Promoting Osteoblast Functions and Inhibiting Bacterial Adhesion. *Biomaterials* 29, 1412–1421. doi:10.1016/j.biomaterials.2007.12.019

Del Hoyo-Gallego, S., Pérez-Álvarez, L., Gómez-Galván, F., Lizundia, E., Kuritka, I., Sedlarik, V., et al. (2016). Construction of Antibacterial Poly(ethylene Terephthalate) Films via Layer by Layer Assembly of Chitosan and Hyaluronic Acid. *Carbohydr. Polym.* 143, 35–43. doi:10.1016/j.carbpol.2016.02.008

Ding, Y., Yang, M., Yang, Z., Luo, R., Lu, X., Huang, N., et al. (2015). Cooperative Control of Blood Compatibility and Re-endothelialization by Immobilized Heparin and Substrate Topography. *Acta Biomater.* 15, 150–163. doi:10.1016/j.actbio.2014.12.014

Dřímalová, E., Velebný, V., Sasinková, V., Hromádková, Z., and Ebringerová, A. (2005). Degradation of Hyaluronan by Ultrasonication in Comparison to Microwave and Conventional Heating. *Carbohyd. Polym.* 61, 420–426. doi:10.1016/j.carbpol.2005.05.035

Feng, Y., Ma, X., Chang, L., Zhu, S., and Guan, S. (2017). Characterization and Cytocompatibility of Polydopamine on MAO-HA Coating Supported on Mg-Zn-Ca alloy. *Surf. Interf. Anal.* 49, 1115–1123. doi:10.1002/sia.6286

Gao, J. H., Guan, S. K., Chen, J., Wang, L. G., Zhu, S. J., Hu, J. H., et al. (2011a). Fabrication and Characterization of Rod-like Nano-Hydroxyapatite on MAO Coating Supported on Mg-Zn-Ca alloy. *Appl. Surf. Sci.* 257, 2231–2237. doi:10.1016/j.apsusc.2010.09.080

Gao, J. H., Guan, S. K., Ren, Z. W., Sun, Y. F., Zhu, S. J., and Wang, B. (2011b). Homogeneous Corrosion of High Pressure Torsion Treated Mg-Zn-Ca alloy in Simulated Body Fluid. *Mater. Lett.* 65, 691–693. doi:10.1016/j.matlet.2010.11.015

Geng, Z., Cui, Z., Li, Z., Zhu, S., Liang, Y., Liu, Y., et al. (2016). Strontium Incorporation to Optimize the Antibacterial and Biological Characteristics of Silver-Substituted Hydroxyapatite Coating. *Mater. Sci. Eng. C* 58, 467–477. doi:10.1016/j.msec.2015.08.061

Hermawan, H., Dubé, D., and Mantovani, D. (2010). Developments in Metallic Biodegradable Stents☆. *Acta Biomater.* 6, 1693–1697. doi:10.1016/j.actbio.2009.10.006

Hiromoto, S., Nozoe, E., Hanada, K., Yoshimura, T., Shima, K., Kibe, T., et al. (2021). *In Vivo* Degradation and Bone Formation Behaviors of Hydroxyapatite-Coated Mg Alloys in Rat Femur. *Mater. Sci. Eng. C* 122, 111942. doi:10.1016/j.msec.2021.111942

Hovgaard, M. B., Rechendorff, K., Chevallier, J., Foss, M., and Besenbacher, F. (2008). Fibronectin Adsorption on Tantalum: the Influence of Nanoroughness. *J. Phys. Chem. B* 112, 8241–8249. doi:10.1021/jp801103n

Huang, Y., Hao, M., Nian, X., Qiao, H., Zhang, X., Zhang, X., et al. (2016). Strontium and Copper Co-substituted Hydroxyapatite-Based Coatings with Improved Antibacterial Activity and Cytocompatibility Fabricated by Electrodeposition. *Ceramics Int.* 42, 11876–11888. doi:10.1016/j.ceramint.2016.04.110

Jou, C.-H., Yuan, L., Lin, S.-M., Hwang, M.-C., Chou, W.-L., Yu, D.-G., et al. (2007). Biocompatibility and Antibacterial Activity of Chitosan and Hyaluronic Acid Immobilized Polyester Fibers. *J. Appl. Polym. Sci.* 104, 220–225. doi:10.1002/app.25549

Kokubo, T., and Takadama, H. (2006). How Useful Is SBF in Predicting *In Vivo* Bone Bioactivity? *Biomaterials* 27, 2907–2915. doi:10.1016/j.biomaterials.2006.01.017

Larkin, A. L., Davis, R. M., and Rajagopalan, P. (2010). Biocompatible, Detachable, and Free-Standing Polyelectrolyte Multilayer Films. *Biomacromolecules* 11, 2788–2796. doi:10.1021/bm100867h

Lee, C. Y., Bae, J.-H., Kim, T.-Y., Chang, S.-H., and Kim, S. Y. (2015). Using Silane-Functionalized Graphene Oxides for Enhancing the Interfacial Bonding Strength of Carbon/epoxy Composites. *Compos. A: Appl. Sci. Manufact.* 75, 11–17. doi:10.1016/j.compositesa.2015.04.013

Li, Y., Li, Q., Zhu, S., Luo, E., Li, J., Feng, G., et al. (2010). The Effect of Strontium-Substituted Hydroxyapatite Coating on Implant Fixation in Ovariectomized Rats. *Biomaterials* 31, 9006–9014. doi:10.1016/j.biomaterials.2010.07.112

Li, H., Jiang, J., Ge, Y., Xu, J., Zhang, P., Zhong, W., et al. (2013). Layer-by-Layer Hyaluronic Acid-Chitosan Coating Promoted New Collagen Ingrowth into a Poly(ethylene Terephthalate) Artificial Ligament in a Rabbit Medical Collateral Ligament (MCL) Reconstruction Model. *J. Biomater. Sci. Polym. Ed.* 24, 431–446. doi:10.1080/09205063.2012.690284

Lichter, J. A., Van Vliet, K. J., and Rubner, M. F. (2009). Design of Antibacterial Surfaces and Interfaces: Polyelectrolyte Multilayers as a Multifunctional Platform. *Macromolecules* 42, 8573–8586. doi:10.1021/ma901356s

Lim, P. N., Chang, L., Tay, B. Y., Guneta, V., Choong, C., Ho, B., et al. (2014). Proposed Mechanism of Antibacterial Action of Chemically Modified Apatite for Reduced Bone Infection. *ACS Appl. Mater. Inter.* 6, 17082–17092. doi:10.1021/am504716g

Lim, P. N., Chang, L., and Thian, E. S. (2015). Development of Nanosized Silver-Substituted Apatite for Biomedical Applications: A Review. *Nanomed. Nanotechnol. Biol. Med.* 11, 1331–1344. doi:10.1016/j.nano.2015.03.016

Lin, K., Xia, L., Li, H., Jiang, X., Pan, H., Xu, Y., et al. (2013). Enhanced Osteoporotic Bone Regeneration by Strontium-Substituted Calcium Silicate Bioactive Ceramics. *Biomaterials* 34, 10028–10042. doi:10.1016/j.biomaterials.2013.09.056

Lin, X., Yang, X., Tan, L., Li, M., Wang, X., Zhang, Y., et al. (2014). *In Vitro* degradation and Biocompatibility of a Strontium-Containing Micro-arc Oxidation Coating on the Biodegradable ZK60 Magnesium alloy. *Appl. Surf. Sci.* 288, 718–726. doi:10.1016/j.apsusc.2013.10.113

Mulligan, K., Jakubek, Z. J., and Johnston, L. J. (2011). Supported Lipid Bilayers on Biocompatible Polysaccharide Multilayers. *Langmuir* 27, 14352–14359. doi:10.1021/la203207p

Olivares-Navarrete, R., Raz, P., Zhao, G., Chen, J., Wieland, M., Cochran, D. L., et al. (2008). Integrin 2 1 Plays a Critical Role in Osteoblast Response to Micron-Scale Surface Structure and Surface Energy of Titanium Substrates. *Proc. Natl. Acad. Sci.* 105, 15767–15772. doi:10.1073/pnas.0805420105

Qiu, K., Zhao, X. J., Wan, C. X., Zhao, C. S., and Chen, Y. W. (2006). Effect of Strontium Ions on the Growth of ROS17/2.8 Cells on Porous Calcium Polyphosphate Scaffolds. *Biomaterials* 27, 1277–1286. doi:10.1016/j.biomaterials.2005.08.006

Rabea, E. I., Badawy, M. E.-T., Stevens, C. V., Smagghe, G., and Steurbaut, W. (2003). Chitosan as Antimicrobial Agent: Applications and Mode of Action. *Biomacromolecules* 4, 1457–1465. doi:10.1021/bm034130m

Ramezanzadeh, B., Ahmadi, A., and Mahdavian, M. (2016). Enhancement of the Corrosion protection Performance and Cathodic Delamination Resistance of Epoxy Coating through Treatment of Steel Substrate by a Novel Nanometric Sol-Gel Based Silane Composite Film Filled with Functionalized Graphene Oxide Nanosheets. *Corrosion Sci.* 109, 182–205. doi:10.1016/j.corsci.2016.04.004

Rehman, S., Khan, K., Mujahid, M., and Nosheen, S. (2016). Synthesis of Nano-Hydroxyapatite and its Rapid Mediated Surface Functionalization by Silane Coupling Agent. *Mater. Sci. Eng. C* 58, 675–681. doi:10.1016/j.msec.2015.09.014

Savard, T., Beaulieu, C., Boucher, I., and Champagne, C. P. (2002). Antimicrobial Action of Hydrolyzed Chitosan against Spoilage Yeasts and Lactic Acid Bacteria of Fermented Vegetables. *J. Food Prot.* 65, 828–833. doi:10.4315/0362-028x-65.5.828

Schrooten, I., Cabrera, W., Goodman, W. G., Dauwe, S., Lamberts, L. V., Marynissen, R., et al. (1998). Strontium Causes Osteomalacia in Chronic Renal Failure Rats. *Kidney Int.* 54, 448–456. doi:10.1046/j.1523-1755.1998.00035.x

Servaty, R., Schiller, J., Binder, H., and Arnold, K. (2001). Hydration of Polymeric Components of Cartilage - an Infrared Spectroscopic Study on Hyaluronic Acid and Chondroitin Sulfate. *Int. J. Biol. Macromol.* 28, 121–127. doi:10.1016/s0141-8130(00)00161-6

Singh, S. S., Roy, A., Lee, B. E., Ohodnicki, J., Loghmanian, A., Banerjee, I., et al. (2014). A Study of Strontium Doped Calcium Phosphate Coatings on AZ31. *Mater. Sci. Eng. C* 40, 357–365. doi:10.1016/j.msec.2014.03.062

Song, X., Chang, L., Wang, J., Zhu, S., Wang, L., Feng, K., et al. (2018). Investigation on the *In Vitro* Cytocompatibility of Mg-Zn-Y-Nd-Zr Alloys as Degradable

Orthopaedic Implant Materials. *J. Mater. Sci. Mater. Med.* 29, 44. doi:10.1007/s10856-018-6050-8

Sun, J., Cao, Z., and Wu, L. (2015). Polyvinylidene Fluoride/silane-Treated Hydroxyapatite Mixed Matrix Membrane for Enzyme Capturing. *Colloids Surf. B: Biointerfaces* 126, 265–272. doi:10.1016/j.colsurfb.2014.12.034

Umerska, A., Paluch, K. J., Inkielewicz-Stępniak, I., Santos-Martinez, M. J., Corrigan, O. I., Medina, C., et al. (2012). Exploring the Assembly Process and Properties of Novel Crosslinker-free Hyaluronate-Based Polyelectrolyte Complex Nanocarriers. *Int. J. Pharm.* 436, 75–87. doi:10.1016/j.ijpharm.2012.07.011

Wang, H. X., Guan, S. K., Wang, X., Ren, C. X., and Wang, L. G. (2010). *In Vitro* degradation and Mechanical Integrity of Mg-Zn-Ca alloy Coated with Ca-Deficient Hydroxyapatite by the Pulse Electrodeposition Process☆. *Acta Biomater.* 6, 1743–1748. doi:10.1016/j.actbio.2009.12.009

Wang, Q., Xu, L., Willumeit-Römer, R., and Luthringer-Feyerabend, B. J. C. (2021). Macrophage-derived Oncostatin M/bone Morphogenetic Protein 6 in Response to Mg-Based Materials Influences Pro-osteogenic Activity of Human Umbilical Cord Perivascular Cells. *Acta Biomater.* 133, 268–279. doi:10.1016/j.actbio.2020.12.016

Xue, W., Hosick, H. L., Bandyopadhyay, A., Bose, S., Ding, C., Luk, K. D. K., et al. (2007). Preparation and Cell-Materials Interactions of Plasma Sprayed Strontium-Containing Hydroxyapatite Coating. *Surf. Coat. Technol.* 201, 4685–4693. doi:10.1016/j.surfcoat.2006.10.012

Yang, Y., He, C., Dianyu E, E., Yang, W., Qi, F., Xie, D., et al. (2020). Mg Bone Implant: Features, Developments and Perspectives. *Mater. Des.* 185, 108259. doi:10.1016/j.matdes.2019.108259

Zarins, J., Pilmane, M., Sidhoma, E., and Salma, I. (2016). Does Local Application of Strontium Increase Osteogenesis and Biomaterial Osteointegration in Osteoporotic and Other Bone Tissue Conditions: Review of Literature. *Acta Chir. Latv.* 16, 17–23. doi:10.1515/chilat-2017-0004

Zhang, W., Cao, N., Chai, Y., Xu, X., and Wang, Y. (2014). Synthesis of Nanosize Single-crystal Strontium Hydroxyapatite via a Simple Sol-Gel Method. *Ceramics Int.* 40, 16061–16064. doi:10.1016/j.ceramint.2014.07.103

Zhao, F., Lei, B., Li, X., Mo, Y., Wang, R., Chen, D., et al. (2018). Promoting *In Vivo* Early Angiogenesis with Sub-micrometer Strontium-Contained Bioactive Microspheres through Modulating Macrophage Phenotypes. *Biomaterials* 178, 36–47. doi:10.1016/j.biomaterials.2018.06.004

Zheng, Y. F., Gu, X. N., Xi, Y. L., and Chai, D. L. (2010). *In Vitro* degradation and Cytotoxicity of Mg/Ca Composites Produced by Powder Metallurgy☆. *Acta Biomater.* 6, 1783–1791. doi:10.1016/j.actbio.2009.10.009

Zhu, H., Yue, L., Zhuang, C., Zhang, Y., Liu, X., Yin, Y., et al. (2016). Fabrication and Characterization of Self-Assembled Graphene Oxide/Silane Coatings for Corrosion Resistance. *Surf. Coat. Technol.* 304, 76–84. doi:10.1016/j.surfcoat.2016.07.002

Conflict of Interest: The authors declare that the research was conducted in the absence of any commercial or financial relationships that could be construed as a potential conflict of interest.

Publisher's Note: All claims expressed in this article are solely those of the authors and do not necessarily represent those of their affiliated organizations, or those of the publisher, the editors, and the reviewers. Any product that may be evaluated in this article, or claim that may be made by its manufacturer, is not guaranteed or endorsed by the publisher.